



Article

Monitoring and Analysis of the Collapse at Xinjing Open-Pit Mine, Inner Mongolia, China, Using Multi-Source Remote Sensing

Nianbin Zhang ^{1,2}, Yunjia Wang ^{1,2,*}, Feng Zhao ^{1,2} , Teng Wang ^{1,2} , Kewei Zhang ^{1,2}, Hongdong Fan ^{1,2}, Dawei Zhou ^{1,2}, Leixin Zhang ^{1,2} , Shiyong Yan ^{1,2}, Xinpeng Diao ^{1,2} and Rui Song ^{1,2}

¹ Key Laboratory of Land Environment and Disaster Monitoring, MNR, China University of Mining and Technology (CUMT), Xuzhou 221116, China; nianbin_zhang@cumt.edu.cn (N.Z.);

feng.zhao@cumt.edu.cn (F.Z.); wteng_611@cumt.edu.cn (T.W.); zkw@cumt.edu.cn (K.Z.); ywfhhd@cumt.edu.cn (H.F.); dwzhou2008@cumt.edu.cn (D.Z.); leixin_zhang@cumt.edu.cn (L.Z.); yanshiyong@cumt.edu.cn (S.Y.); xpiao@cumt.edu.cn (X.D.); rui_song@cumt.edu.cn (R.S.)

² School of Environment Science and Spatial Informatics, China University of Mining and Technology (CUMT), Xuzhou 221116, China

* Correspondence: wyj4139@cumt.edu.cn

Abstract: The collapse of open-pit coal mine slopes is a kind of severe geological hazard that may cause resource waste, economic loss, and casualties. On 22 February 2023, a large-scale collapse occurred at the Xinjing Open-Pit Mine in Inner Mongolia, China, leading to the loss of 53 lives. Thus, monitoring of the slope stability is important for preventing similar potential damage. It is difficult to fully obtain the temporal and spatial information of the whole mining area using conventional ground monitoring technologies. Therefore, in this study, multi-source remote sensing methods, combined with local geological conditions, are employed to monitor the open-pit mine and analyze the causes of the accident. Firstly, based on GF-2 data, remote sensing interpretation methods are used to locate and analyze the collapse area. The results indicate that high-resolution remote sensing can delineate the collapse boundary, supporting the post-disaster rescue. Subsequently, multi-temporal Radarsat-2 and Sentinel-1A satellite data, covering the period from mining to collapse, are integrated with D-InSAR and DS-InSAR technologies to monitor the deformation of both the collapse areas and the potential risk to dump slopes. The D-InSAR result suggests that high-intensity open-pit mining may be the dominant factor affecting deformation. Furthermore, the boundary between the collapse trailing edge and the non-collapse area could be found in the DS-InSAR result. Moreover, various data sources, including DEM and geological data, are combined to analyze the causes and trends of the deformation. The results suggest that the dump slopes are stable. Meanwhile, the deformation trends of the collapse slope indicate that there may be faults or joint surfaces of the collapse trailing edge boundary. The slope angle exceeding the designed value during the mining is the main cause of the collapse. In addition, the thawing of soil moisture caused by the increase in temperature and the reduction in the mechanical properties of the rock and soil due to underground voids and coal fires also contributed to the accident. This study demonstrates that multi-source remote sensing technologies can quickly and accurately identify potential high-risk areas, which is of great significance for pre-disaster warning and post-disaster rescue.



Citation: Zhang, N.; Wang, Y.; Zhao, F.; Wang, T.; Zhang, K.; Fan, H.; Zhou, D.; Zhang, L.; Yan, S.; Diao, X.; et al. Monitoring and Analysis of the Collapse at Xinjing Open-Pit Mine, Inner Mongolia, China, Using Multi-Source Remote Sensing. *Remote Sens.* **2024**, *16*, 993. <https://doi.org/10.3390/rs16060993>

Academic Editor: Giuseppe Casula

Received: 26 January 2024

Revised: 1 March 2024

Accepted: 6 March 2024

Published: 12 March 2024



Copyright: © 2024 by the authors. Licensee MDPI, Basel, Switzerland. This article is an open access article distributed under the terms and conditions of the Creative Commons Attribution (CC BY) license (<https://creativecommons.org/licenses/by/4.0/>).

Keywords: multi-source remote sensing; D-InSAR; DS-InSAR; surface deformation; open-pit mine

1. Introduction

Open-pit mining has the advantages of a short construction period, large mining scale, low production cost, and high resource recovery rate [1]. China has abundant open-pit coal reserves, constituting 10–15% of the total coal reserves, mainly concentrated in the Inner Mongolia, Shanxi, Xinjiang, and Yunnan provinces [2]. However, the risk of geological

hazards, such as landslides and collapses, increases with the ongoing deepening of open-pit mines [3–5]. Therefore, monitoring the open-pit mining areas is of great significance.

The slope ground monitoring methods of open-pit mines include leveling, GNSS, total station, slope radar, etc. [6–8]. These methods have high precision but are also plagued by low efficiency, limited monitoring points, and the challenge of comprehensively monitoring the entire open-pit mine [9,10]. As an active microwave remote sensing technology, SAR (Spaceborne Synthetic Aperture Radar) interferometry offers broad coverage, frequent revisits, and significant economic benefits. It is widely used in urban subsidence and mining area monitoring and other fields [11–15]. D-InSAR (Differential Interferometric Synthetic Aperture Radar) technology is employed to monitor open-pit mines and has been verified to have good consistency compared to leveling results [16,17]. However, due to temporal and spatial incoherence caused by long monitoring periods or substantial terrain modifications, it is difficult to obtain high-accuracy measurement results with D-InSAR [18,19]. This limitation is alleviated to some extent by conventional time-series PS-InSAR (Permanent Scatterer InSAR) [20,21] and SBAS-InSAR (Small Baseline Subset InSAR) [22,23]. Nevertheless, these methods primarily rely on permanent scatterers such as buildings, which makes it challenging to obtain sufficient monitoring points in suburban open-pit mines. DS-InSAR (Distributed Scatterer InSAR), capable of identifying distributed scatterer points in non-urban areas, emerges as a solution to increase the density of monitoring points [24–26]. It has been applied to capture the time-series ground deformation of open-pit mining areas in Anshan, China, demonstrating its superiority in point selection compared to conventional time-series InSAR [27].

The stability of open-pit mine slopes is mainly influenced by local geological structures [28,29], lithology [30], water [31–33], blasting vibration [34], the slope geometry [35], and other mining activities [36,37], resulting in high uncertainty. Currently, the monitoring of the open-pit mines relies on a single data source, which may only partially reflect the spatio-temporal variations in the mining area when data are missing. Furthermore, it is difficult to accurately and promptly delineate the extent of landslides or collapses based solely on deformation. Optical remote sensing can overcome these limitations and guide rescue operations. Therefore, employing a comprehensive approach, based on multi-source remote sensing, is crucial to systematically analyzing the spatio-temporal variations in open-pit mining areas and preventing potential geological hazards.

On 22 February 2023, a large-scale, severe collapse occurred in the Xinjing Open-Pit Mine in Inner Mongolia, China, leading to the loss of 53 lives and causing direct economic losses amounting to about USD 28.38 million [38]. Scholars have conducted research on the accident using multi-source remote sensing technologies. Specifically, Wu et al. [39] and An et al. [40] employed high-resolution optical data to delineate the collapse range of the Xinjing Open-Pit Mine in Inner Mongolia. They also utilized Sentinel-1A data to obtain the spatio-temporal deformation. However, due to the absence of Sentinel-1A data for several months before the collapse, monitoring and analyzing the spatio-temporal changes comprehensively before the accident is challenging. Moreover, they did not conduct a more in-depth analysis of the deformation trends by integrating local geological and survey data.

In this study, multi-source remote sensing data were employed to monitor and analyze the collapse and dump areas in the Xinjing Open-Pit Mine. This article is organized as follows. Section 2 explains the study area and the data used for this study. Section 3 describes the method of D-InSAR and DS-InSAR techniques. In Section 4, the results are described and analyzed. Section 5 discusses the major causes of the collapse and explores the correlation between deformation and the division of the collapse stages, while Section 6 concludes this study.

2. Study Area and Datasets

2.1. Study Area

As shown in Figure 1, the Xinjing Open-Pit Mine, covering an area of about 1.3448 km², is located approximately 88 km south of Bayannur Town, Alashan Left Banner, Inner

Mongolia, China, with coordinates between 105.639°E – 105.681°E and 37.956°N – 37.993°N . The mining history can be traced back to 1958, when the small-scale coal mine extraction method was used. Since then, mining methods have undergone technological transformations, and new mining methods, such as longwall coal mining and horizontal layered caving, have emerged. However, coal fires have been formed with the mining. A fire suppression initiative was launched in 2010, spanning from the southern to the northern regions of the mining area, and was completed by the end of 2012. Moreover, the official transition to open-pit mining with a single-bucket and truck process began in January 2021. The designed duration of service was 3.5 years, with a production scale of 900,000 tons per year. Subsequently, the site comprised one open-pit mining area and four dumps.

The mine is located in a low, mountainous area with exposed bedrock and sparse vegetation belonging to the plateau erosion hilly landform. The strike direction of the mining area is approximately 295° , and the dip direction is approximately 25° . It is primarily characterized by a single anticline structure with several small-scale faults in the region. The elevation of the mining site ranges from 1050 m to 1493 m.

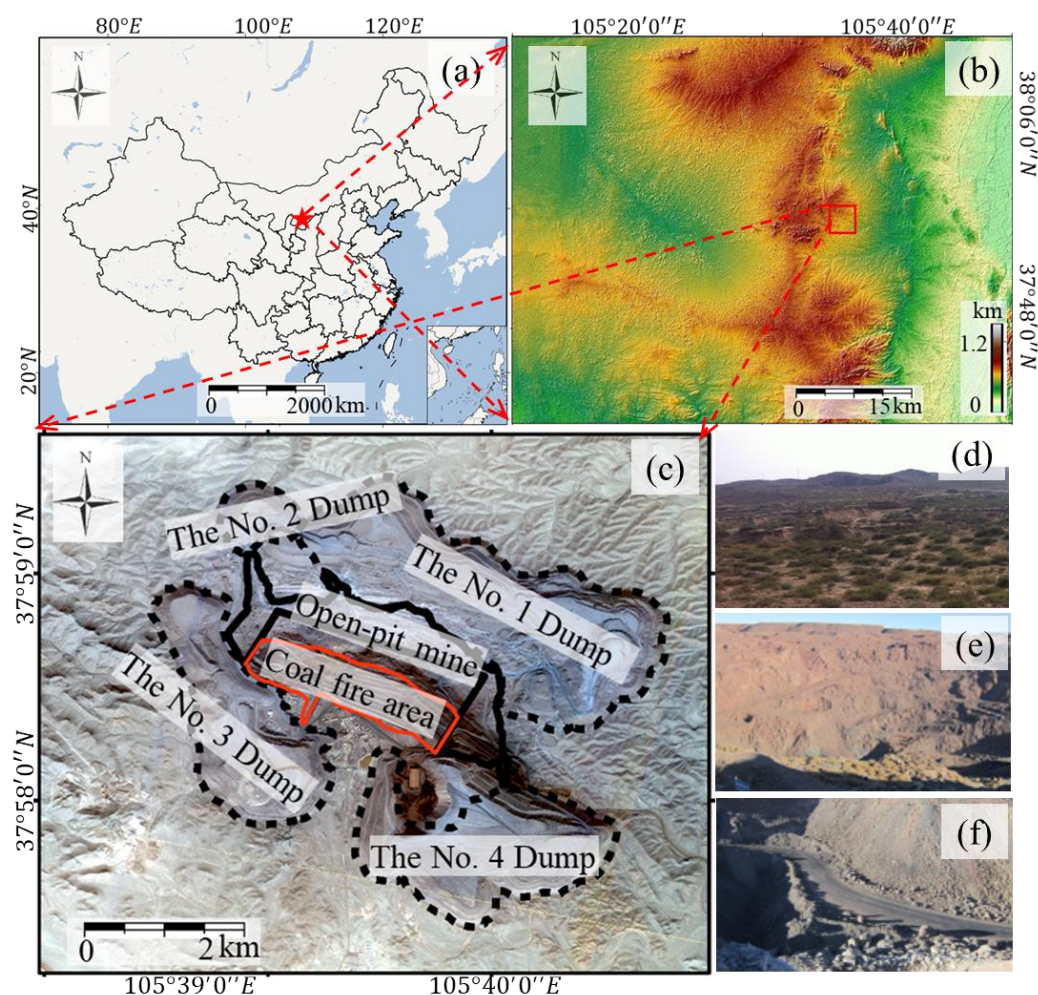


Figure 1. Sketch map of the study area. (a) is the geographical location of study area; (b) is the DEM of the study area derived from SRTM data; (c) is the spatial distribution of the mine provided by GF-2; (d) is the natural landscape of the mine; (e) is the open-pit mining area; and (f) is the coal haulage road.

2.2. Datasets

2.2.1. GF-2

Two GF-2 optical data images, collected on 16 February 2023 and 23 February 2023, were used to delineate the landslide collapse area. The GF-2 satellite is the first civilian

optical remote sensing satellite independently developed by China with a spatial resolution better than 1 m. It is equipped with two high-resolution 1 m panchromatic and 4 m multispectral cameras with a fusion resolution of $0.8 \text{ m} \times 0.8 \text{ m}$ [41].

2.2.2. Radarsat-2

As shown in Table 1, two Radarsat-2 images from 10 January 2023 and 3 February 2023 were used to obtain the deformation near the collapse time. Radarsat-2 is a high-resolution radar satellite equipped with C-band sensors with a resolution of $3 \text{ m} \times 3 \text{ m}$. The satellite has an imaging width of 125 km with a revisit period of 24 days [42]. The incidence angle is approximately 35.29° in this region and the data coverage is shown in Figure 2.

Table 1. Sentinel-1A and Radarsat-2 data parameters.

Satellites	Incidence Angle ($^\circ$)	Resolution (m)		Time
		Range	Azimuth	
Radarsat-2	35.29	3	3	10 January 2023–3 February 2023
Sentinel-1A	39.12	2.3	13.9	7 January 2021–11 August 2022

2.2.3. Sentinel-1A

Thirty-five ascending Sentinel-1A images obtained during the mining period were utilized to capture the deformation of the open-pit mine. Operated by the European Space Agency (ESA), Sentinel-1A was launched on 2 April 2014, and the satellite revisiting period was 12 days. As shown in Table 1, in the study area, the incidence angles were approximately 39.12° , and the resolution was 2.3 m by 13.9 m. The acquisition time was from 7 January 2021 to 11 August 2022 and data coverage is shown in Figure 2. All data could be downloaded freely from the Alaska Satellite Facility (ASF) [43].

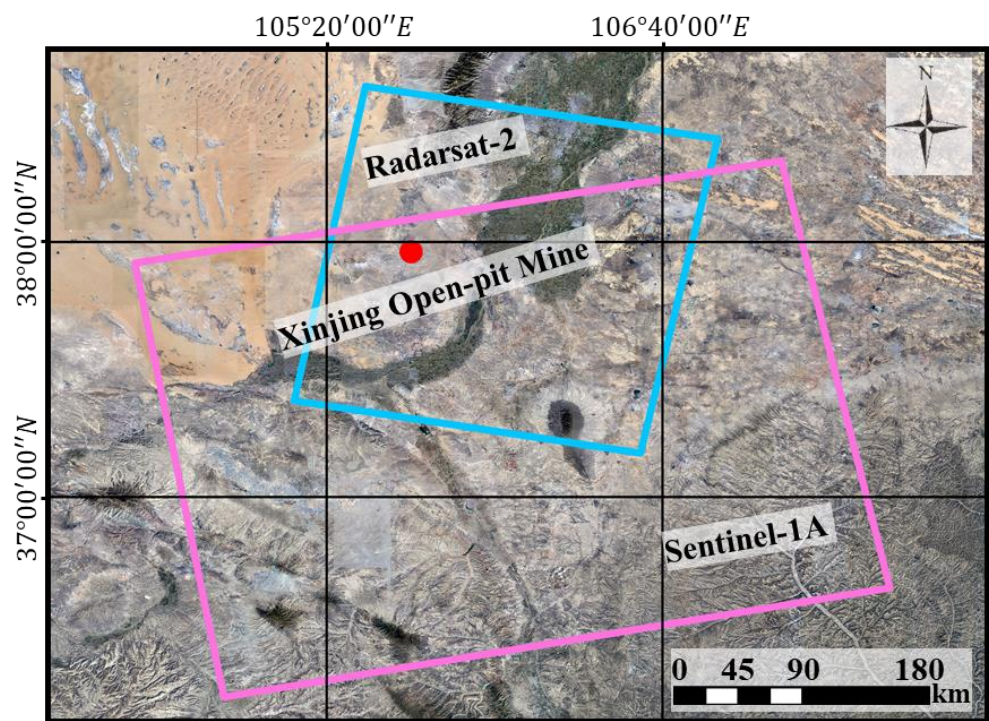


Figure 2. The Radarsat-2 and Sentinel-1A satellite data coverage.

3. Methods

3.1. Differential InSAR

D-InSAR utilizes the phase information from SAR complex images to obtain surface deformation. An interferogram is generated by multiplying two SAR images with their conjugates. The interferometric phase φ is mainly composed of the following parts [44,45]:

$$\varphi = \varphi_{defo} + \varphi_{topo} + \varphi_{flat} + \varphi_{atmo} + \varphi_{noise} \quad (1)$$

where φ_{defo} is the deformation phase in the line of sight (LOS) direction, φ_{topo} is the topographic phase, φ_{flat} is the flat phase, φ_{atmo} is the atmospheric phase, and φ_{noise} is the noise phase. The main processing workflow includes reference and secondary image coregistration, interferogram generation, filtering, phase unwrapping, geocoding, deformation extraction, etc. In the process, the last three terms of Equation (1) could be suppressed or removed.

In this study, the two-track differential interference method was utilized for the Radarsat-2 data processing. Details were as follows. The two images were coregistered and cropped to a pixel count of 2000×3600 . Subsequently, SRTM data with a resolution of 30 m were used as an external DEM to remove the terrain phase. The study area was small, and the influence of atmospheric errors could be ignored [11]. Meanwhile, an adaptive filter with a value of 0.6 was applied to minimize noise. Furthermore, pixels with coherence below 0.3 were masked, and the phase unwrapping process was then carried out using the minimum cost flow method. The surface deformation was subsequently derived.

3.2. Distributed Scatterer InSAR

As shown in Figure 3, the key stages of DS-InSAR processing comprise reference and secondary image coregistration, interferogram generation, homogeneous pixel identification, phase optimization, point selection, and deformation parameter estimation [46,47]. Compared with the conventional time-series InSAR, two steps of DS homogeneous pixel identification and phase optimization are added in point selection, which will be summarized below.

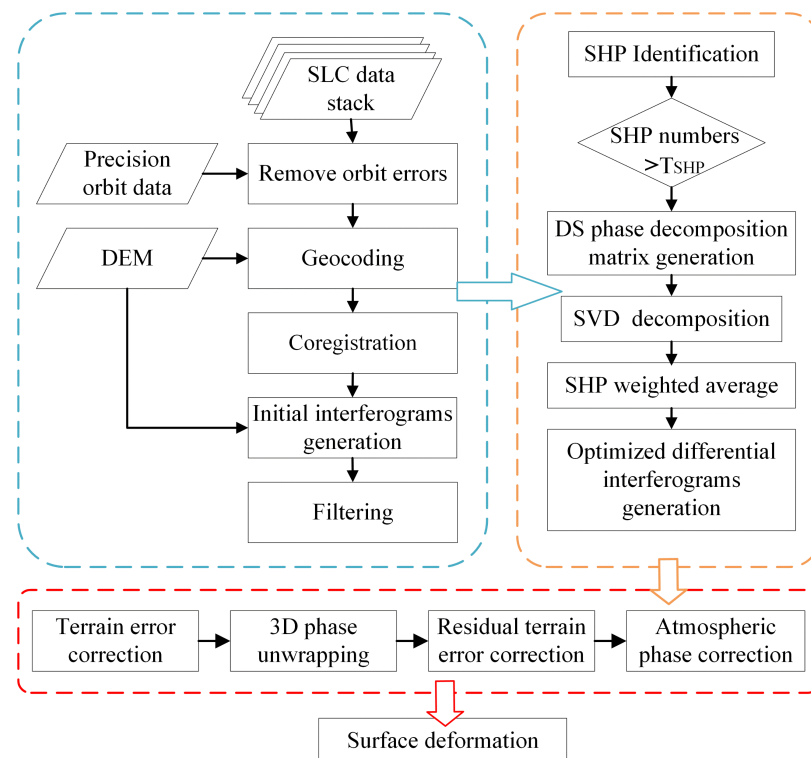


Figure 3. DS-InSAR processing flowchart.

3.2.1. Fast Statistically Homogeneous Pixel Identification

Fast Statistically Homogeneous Pixel Selection (FaSHPS), a parametric test, is a method for quickly selecting statistically homogeneous pixels [48]. It has the advantages of low heterogeneity and rapid identification speed, leading to its widespread adoption. FaSHPS aims to swiftly identify pixels with similar statistical characteristics in a given confidence interval level, and this capability contributes to efficiently identifying homogeneous regions. According to the theory, the amplitude of a single-look SAR image follows the Rayleigh distribution in homogeneous regions, and the coefficient of variation is constant. The FaSHPS method can be finally expressed as follows:

$$P \left\{ \begin{array}{l} \mu_{(p)} - Z_{1-\frac{\alpha}{2}} 0.52 \frac{\mu_{(p)}}{\sqrt{NL}} < \bar{A}(p) \\ < \mu_{(p)} + Z_{1-\frac{\alpha}{2}} 0.52 \frac{\mu_{(p)}}{\sqrt{NL}} \end{array} \right\} = 1 - \alpha. \quad (2)$$

where $Z_{1-\frac{\alpha}{2}}$ is the $\frac{(1-\alpha)}{2}$ percentile of the standard normal probability density function. $\mu_{(p)}$ represents expectation, N is the number of SAR images in the time series, $\bar{A}(p)$ represents the mean value of the SAR image amplitude, $(1 - \alpha)$ is a given confidence level, and “ L ” represents the looks of the SAR images.

3.2.2. Distributed Scatterer Phase Optimization

The core idea of DS phase optimization is to optimize the phase of DS pixels utilizing homogenous pixels through the principal component analysis method of singular value decomposition [49]. Specifically, a two-dimensional matrix H with dimensions $M \times N$ is generated based on the number of homogeneous pixels in the reference pixels (the DS pixels to be optimized) M and the number of time-series interferograms N . Then, the matrix H undergoes singular value decomposition as follows:

$$H = \sum_{i=1}^k s_i u_i v_i^T. \quad (3)$$

where k is the number of non-zero singular values of the matrix H , and u_i and v_i are the column vectors of the left and right orthogonal matrices in the singular value decomposition of H , respectively. In order to obtain the optimal phase of the final DS, the largest singular value and its corresponding left and right singular vectors u_1 and v_1 are first utilized to produce the noise-reduced matrix $H' = s_1 u_1 v_1^T$. Then, the n th row is extracted as the new reference pixel phase value to generate the optimized interferograms. Finally, the coherence of the decomposed interferograms is calculated, and it is used to obtain a weighted average of the DS homogeneous pixels for the final DS-optimized interferometric phase, as shown in Equation (4).

$$\varphi_{ref} = \frac{\sum_{i=1}^n \varphi_i Coh_i}{\sum_{i=1}^n Coh_i}. \quad (4)$$

where φ_{ref} is the reference pixel phase value, Coh_i is the coherence of the estimated pixel, and φ_i is the homogeneous pixel phase value.

3.2.3. DS-InSAR Data Processing

The number of pixels was cropped to 5000×1000 due to the extensive range of the original image, and then the SAR image acquired on 7 January 2022 was selected as the super master image. The SRTM with 30 m resolution was utilized as the external DEM data for geocoding and coregistration. Ninety-six interferograms were generated using the SBAS method, in which the temporal baseline threshold was set to 120 days, and the perpendicular baseline threshold was set to 150 m (as shown in Figure 4). Additionally, pixels with a connected SHP (fast statistically homogeneous) count exceeding the threshold of 20 were considered as candidates for distributed targets (DSC) in the subsequent phase’s optimized operation. Subsequently, the coherence matrix was calculated, and a weighted

average filtering technique, as mentioned above, was applied to obtain the optimized phase [25]. The Temporal Phase Coherence (TPC) method was then employed with a threshold of 0.6 to select the final DS points [49]. Ultimately, the surface deformation was obtained.

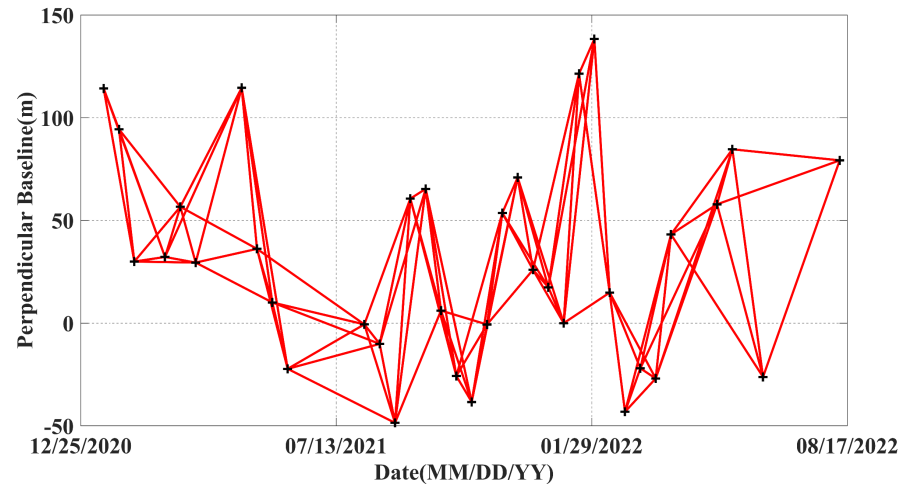


Figure 4. Temporal and perpendicular baseline of distribution used in this study.

4. Results

4.1. Collapse Area Delineation

The high-resolution, enlarged GF-2 images of the partial collapse area, the on-site image, and the topographic profile images before and after the collapse [38] are presented in Figure 5. As shown in Figure 5d, three main elevation steps were identified before the collapse, situated at the elevations of 1515 m, 1435 m, and 1375 m. The maximum accumulated height difference in the collapse area was approximately 285 m. As shown in Figure 5a, it was evident that normal mining operations were ongoing until five days prior to the collapse. Based on Figure 5a and the local topographic profile shown in Figure 5d, it could be observed that the work vehicles were mainly distributed at the bottom of the open-pit mine and on the elevation of the 1375 m platform, approximately 140 m above the ground. The width of this platform was approximately 120 m.

Comparing Figure 5a,b, differences between the two images before and after the collapse could be found. The collapse area, delineated through remote sensing interpretation, revealed an overall region measuring approximately 630 m in length from north to south and 520 m in width from east to west. Moreover, it could be seen from Figure 5b,c that there was a clear boundary line between the collapse trailing edge and the surrounding buried area. Furthermore, the collapse trailing edge exhibited strong reflections due to exposed bedrock [50]. Additionally, irregular “mounds” within the buried area are visible in Figure 5b. When considered alongside Figure 5e, it became apparent that the mound within the buried area primarily originated from the side rock and soil mass, while the discarded materials generated during the mining process represented a small proportion. It is worth noting that the greatest thickness of the buried mound measured approximately 105 m and was situated at the bottom of the valley. These results demonstrate that optical remote sensing can be used to delineate a collapse boundary accurately. When combined with local data, the burial areas of vehicles and people can be identified, thereby assisting in guiding rescue.

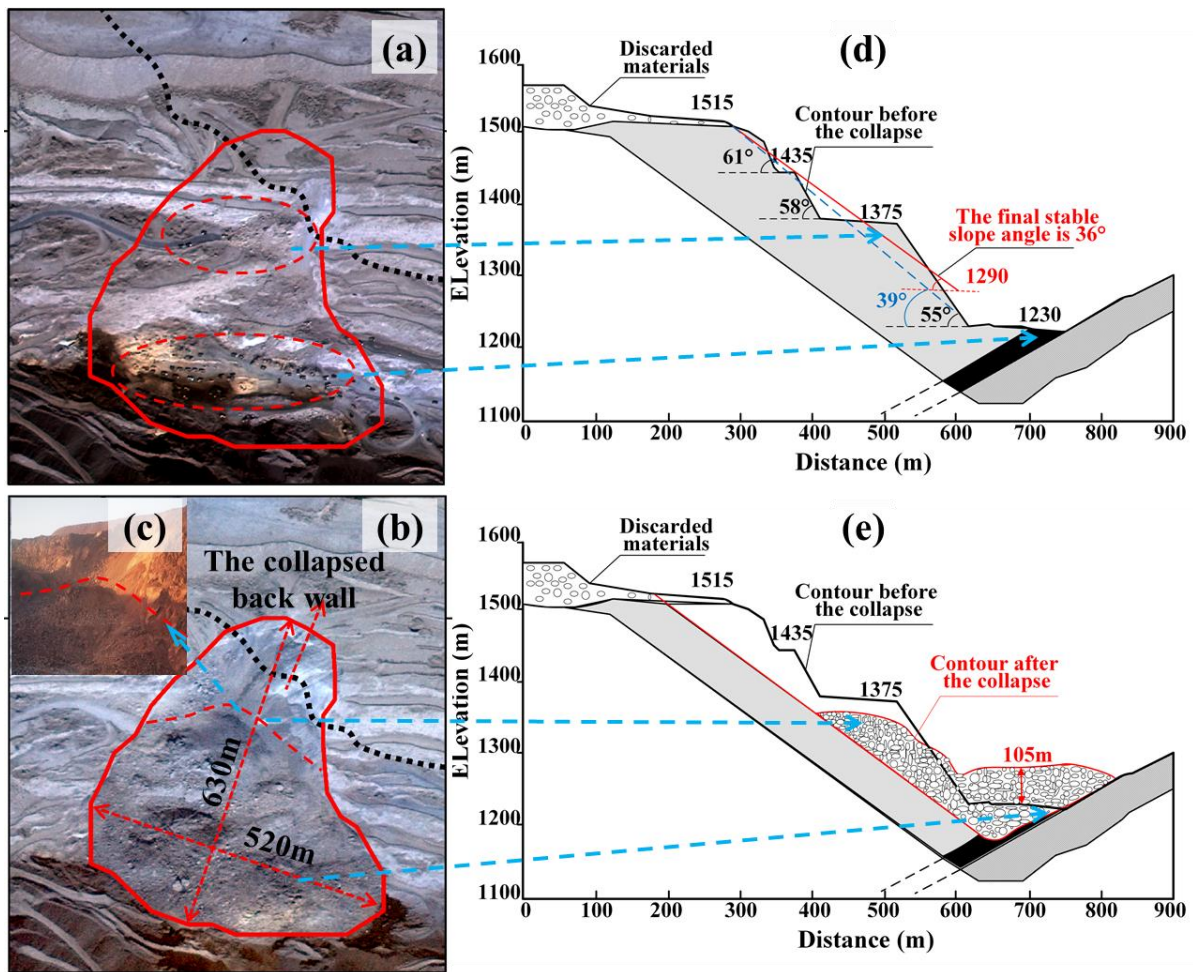


Figure 5. Partial enlargement before and after the accident at the Xinjing Open-Pit Mine (the red polygon is the collapse area). (a) is the optical image before the collapse on 18 February 2023; (b) is the optical image after the collapse on 23 February 2023; (c) is the on-site image after the collapse; (d,e) are the local terrain profiles before and after the collapse.

4.2. D-InSAR Deformation Analysis

The D-InSAR deformation results of Radarsat-2 are illustrated in Figure 6. The mining area exhibited varying degrees of deformation from 10 January 2023 to 3 February 2023. Specifically, the deformation range was mainly distributed in the mining area, as well as in the southeastern region of the No. 1 dump, the southeastern region of the No. 3 dump, and the central and northern regions of the No. 4 dump (as shown in Figure 6a, areas 1–3). The maximum deformation value was approximately -75 mm, concentrated in the open-pit mining area and the central and northern regions of the No. 4 dump. The deformation values for the other dumps ranged from -40 mm to 13 mm. By considering the optical images shown in Figures 6b,c and 7c, it could be seen that there were vehicles present in the deformed areas, indicating that the magnitude of deformation was primarily influenced by mining-related activities. Conversely, areas without mining-related activities displayed no or smaller deformation, suggesting relative stability.

In order to investigate the deformation pattern of the collapse area and the central and northern regions of the No. 4 dump, a local enlarged view was examined, shown in Figure 7. It could be seen from Figure 7a that the deformation values of the valley and the south flank of the collapsed and buried area were larger. In contrast, the deformation values of the north flank were relatively small. Moreover, in the central and northern parts of the No. 4 dump, the maximum deformation values ranged from -60 mm to -80 mm.

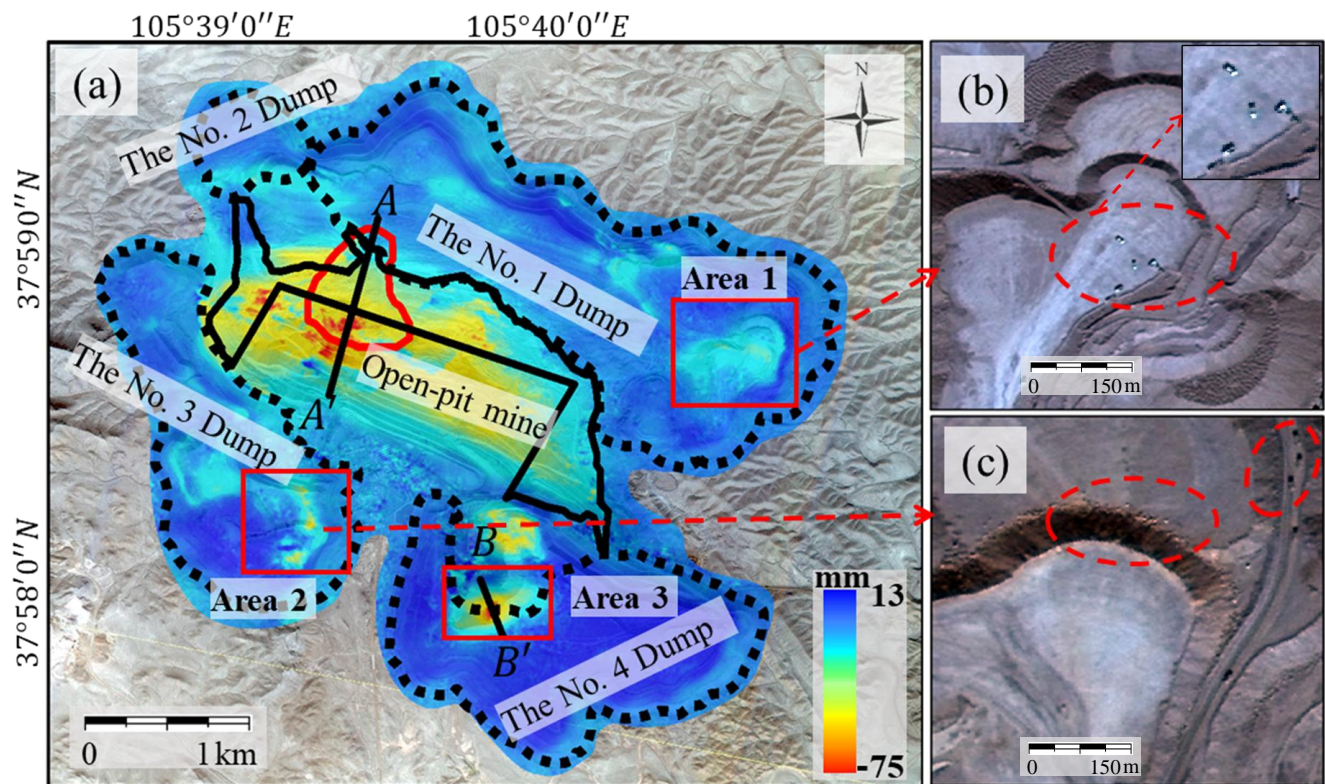


Figure 6. Radarsat-2 D-InSAR deformation maps from 10 January 2023 to 3 February 2023. (a) is the overall deformation map of the open-pit mine; (b,c) are the partially magnified optical images of the No. 3 and No. 4 dumps.

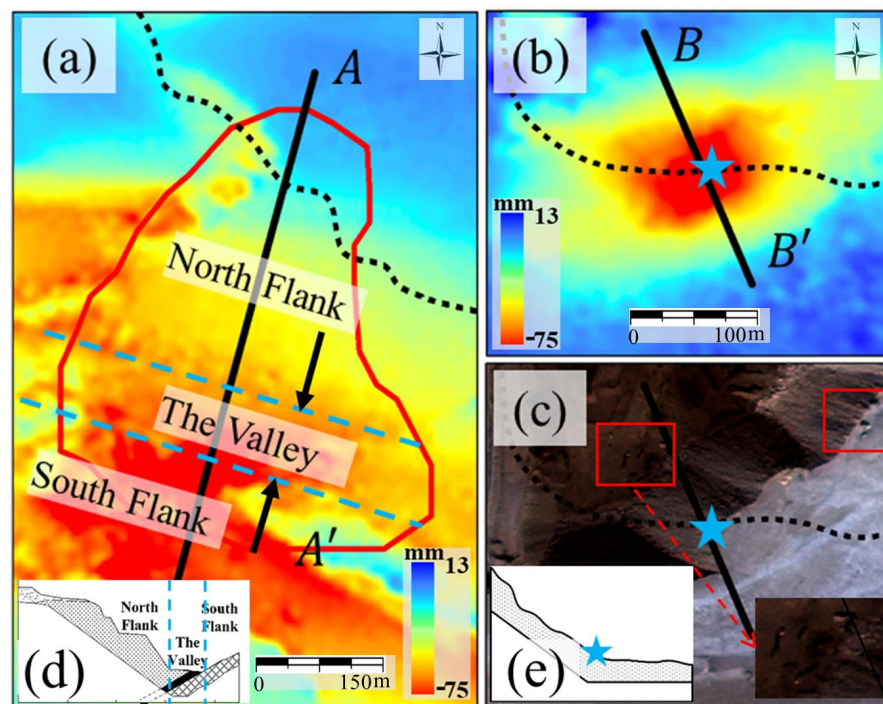


Figure 7. The detailed enlargement map of the open-pit mine. (a,b) are the deformation of the collapse area and the partial area of the No. 4 dump; (c) is the partial optical image of the No. 4 dump; (d,e) are the schematic diagrams of the local terrain profiles.

Profile lines were extracted along the direction of the collapse and slope to examine the deformation patterns in the collapse area (Figure 7a) and the No. 4 dump (Figure 7b). The digital elevation model (DEM) was overlaid onto the resulting deformation profile, as depicted in Figure 8.

As shown in Figure 8, it was evident that the overall deformation trend was irregular. Firstly, the deformation trend was relatively gradual in the north side area where the collapse occurred. The deformation value progressively increased as it moved along the north side boundary towards the bottom of the valley, ranging from -10 mm to -45 mm. The deformation trend on the south side was irregular, exhibiting a pattern of slow–sharp–slow deformation features. The maximum deformation value of -70 mm was located slightly to the south side at the center of the valley bottom.

Additionally, it was observed that the cumulative height difference in the north side area was about 285 m, and there was a 120 m wide platform halfway up the mountain (as shown in Figure 5d). However, the trend of deformation was not clear along the undulating terrain. Specifically, while the elevation trend was changing, the deformation trend remained approximately linear. Similarly, the elevation increased linearly in the south side area, but the deformation trend demonstrated a slow–sharp–slow pattern, indicating a weak correlation with the terrain. However, deformation values increased as they approached the open-pit mining area at the valley bottom regardless of whether it was on the northern or southern side, suggesting that high-intensity open-pit mining may be the dominant factor affecting deformation.

The profile line of the slope of the No. 4 dump exhibited a roughly symmetrical pattern around the maximum deformation value of -70 mm. The maximum deformation value was observed near the bottom of the slope, and the deformation trend appeared linear. Although mining-related activities were also taking place at the No. 4 dump, it could be seen from the topographic profile that the slope had a gentle angle of about 17° , indicating low-risk landslide conditions.

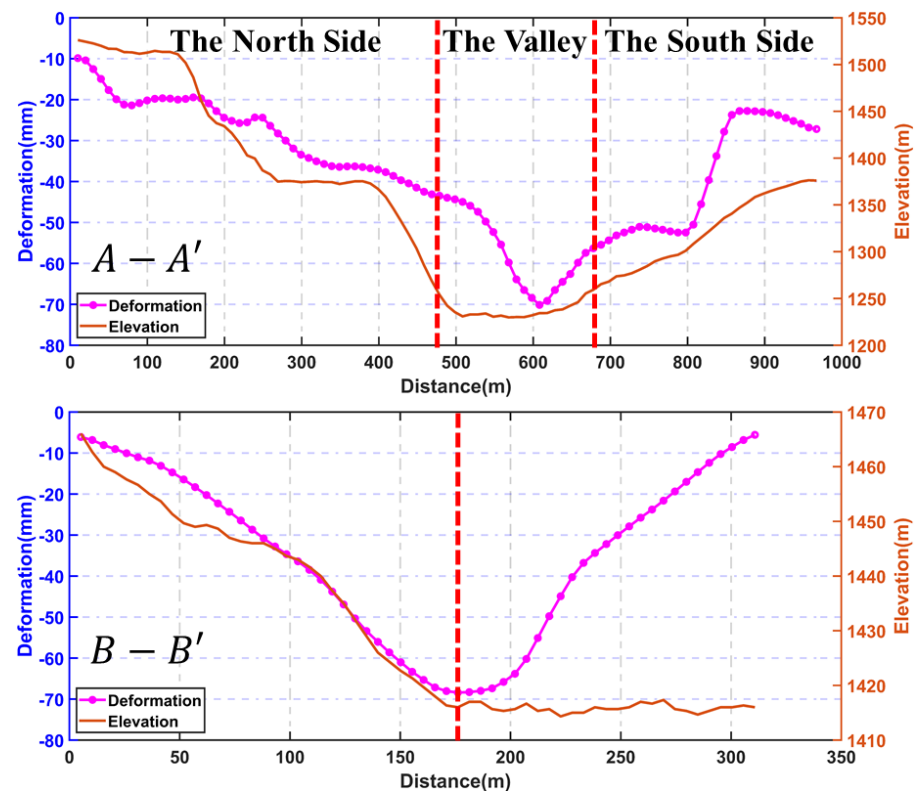


Figure 8. Deformation and elevation profiles of the collapse area and the partial area of the No. 4 dump (the red dashed line represents the regional boundary).

4.3. DS-InSAR Deformation Analysis

DS-InSAR was employed to acquire time-series cumulative deformation data to analyze the spatio-temporal variation trend of the entire mining area. The time-series deformation diagrams of the study area are depicted in Figure 9.

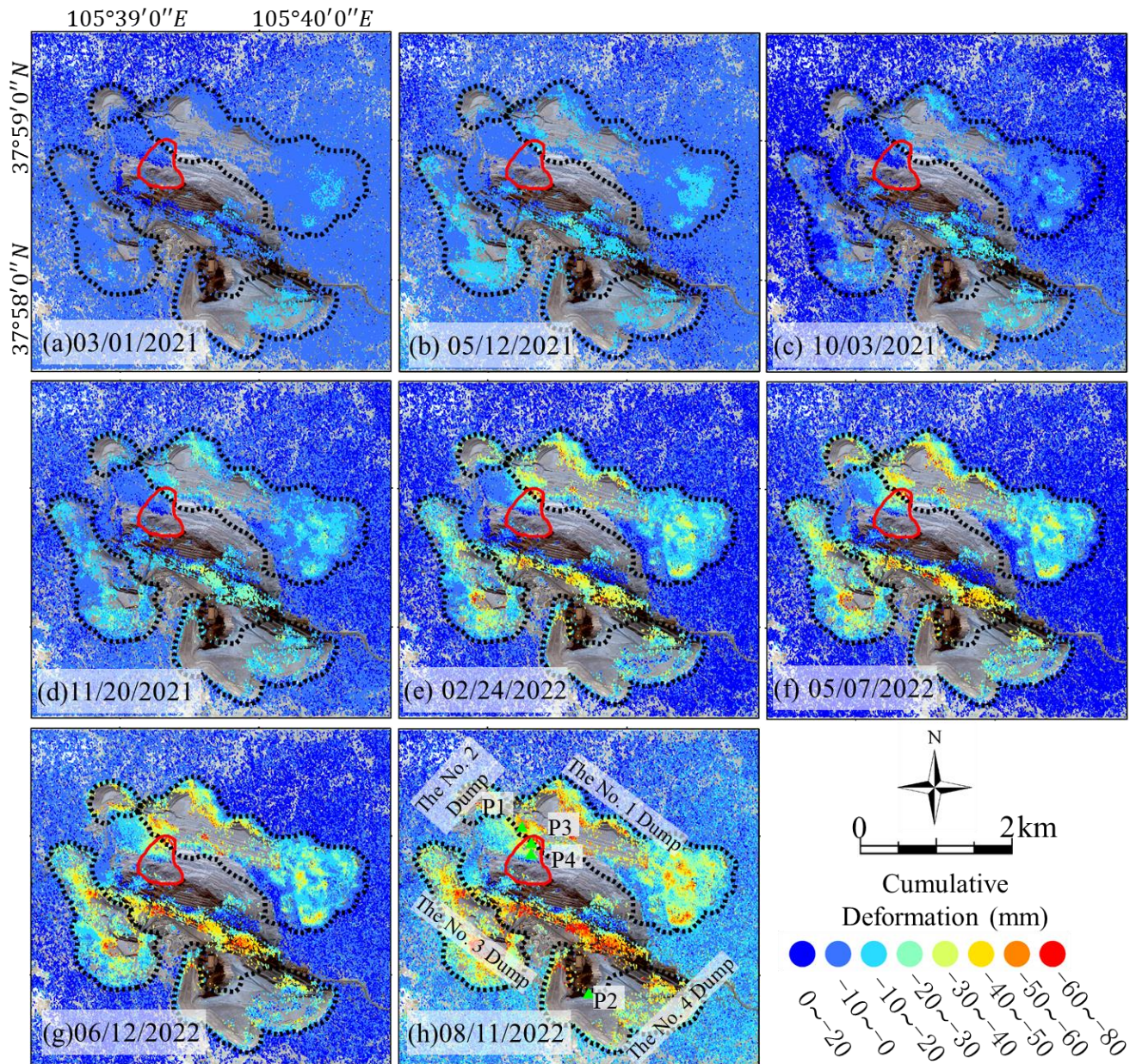


Figure 9. Time-series cumulative deformation diagrams of the Xinjing Open-Pit Mine.

As shown in Figure 9, various levels of deformation were observed within the open-pit mining area. A higher density of points was selected in the southeast of the No. 1 and No. 3 dumps. In contrast, the selected points in the northwest of the No. 1, No. 2, and No. 4 dumps were relatively sparse and primarily concentrated near the slope. The limited number of monitoring points may be attributed to the mining activities on the surface since January 2021. Severe ground damage led to the loss of coherence, making selecting effective monitoring points challenging. The cumulative deformation values of the dump slopes ranged from -60 mm to -80 mm. Figure 9 demonstrates that the monitoring points in the collapse area were primarily concentrated on the the collapse trailing edge. The deformation trend gradually decreased from the north to the south, and a distinct

boundary was observed between the collapse trailing edge and the non-collapsed area. Moreover, the cumulative deformation gradually decreased inward from the collapse trailing edge.

As shown in Figure 9g, four typical points were chosen for temporal analysis. Specifically, P1 was situated in the maximum deformation area of the No. 1 dump slope, P2 was located on the No. 4 dump slope, and P3 and P4 were in the collapse area. The deformation velocity is obtained by dividing the accumulated deformation between two scenes by the time interval. The time-series deformation and velocity results are depicted in Figure 10.

The deformation patterns of points P1 and P2 on the dump slope were prominently linear, as shown in Figure 10a. The velocities at these points remained relatively stable throughout the monitoring period, ranging from -0.05 mm/day to -0.15 mm/day, except for the T1 period (4 August 2021–9 September 2021), when the maximum velocity at P2 reached -0.2 mm/day. Additionally, the velocity trends of points P1 and P2 were parallel before the T1 period. However, a noticeable divergence in the deformation rate trends between these two points occurred after the T1 period. The potential reason may be that the dump site where P2 was located conducted mining activities after the T1 period.

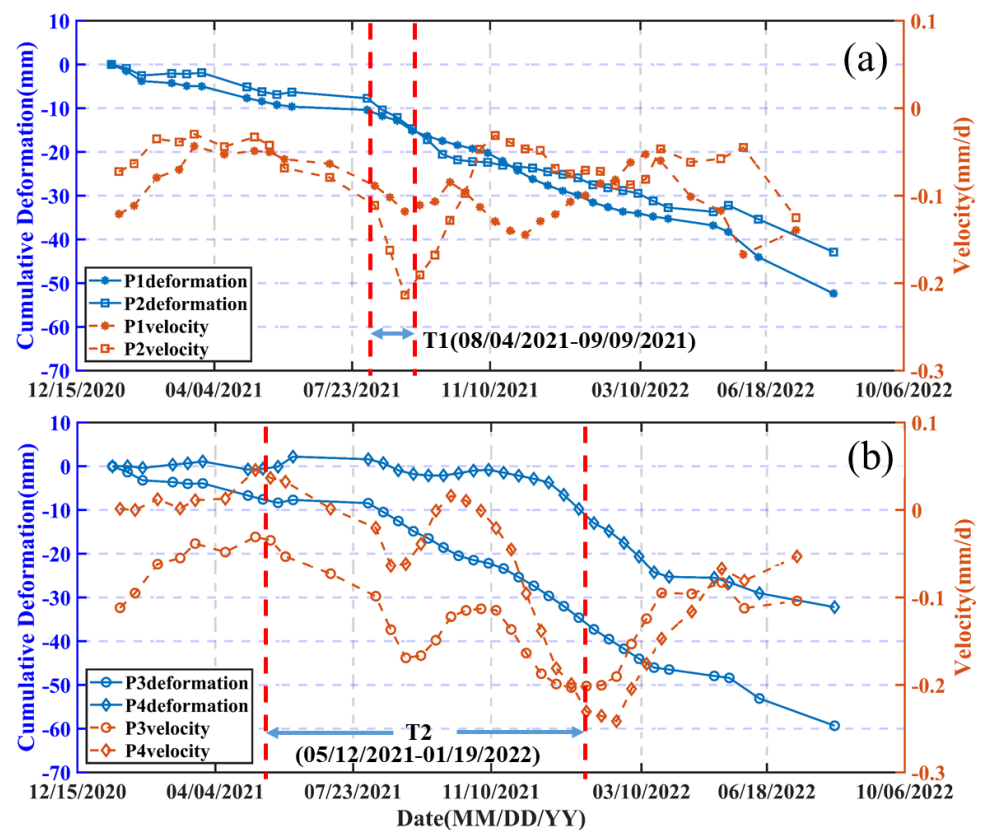


Figure 10. Typical points of time-series deformation and velocity curves. ((a,b) are the deformation and velocity at points P1, P2, P3 and P4).

For points P3 and P4 in the collapse area, the maximum cumulative deformation was -60 mm and -30 mm, respectively. The deformation rate exhibited a more pronounced fluctuation than at points P1 and P2, ranging between approximately 0 mm/day and -0.25 mm/d. In addition, the deformation at P4 occurred later than at P3. Specifically, before the T2 period (12 May 2021–19 January 2022), P3 deformed slowly, while P4 exhibited minimal deformation. During the T2 period, the deformation trends were the same, but the deformation rate of P3 was significantly greater than that of P4. After the T2 period, the deformation rate of P4 surpassed that of P3, reaching a maximum rate of -0.25 mm/day. The reason for this phenomenon will be further discussed in the next section.

5. Discussion

5.1. Main Causes of the Accident

According to the official report, the primary cause of the accident was that the open-pit mining was not conducted according to the prescribed design. Specifically, the benches were modified casually, resulting in an excessively steep and high slope. The final stable slope angle of the mine was 36° , with a calculated slope stability coefficient of 4.287, meeting safety reserve requirements. However, in actuality, the maximum vertical height of the slope was approximately 300 m, leading to an overall slope angle of 39° . In some areas, the slope angle reached as high as 61° , with a corresponding calculated slope stability coefficient of 0.982, indicating an unstable state [38], as shown in Figure 5d. Furthermore, continuous intensive coal stripping at the bottom of the stope contributed to the decreasing slope stability. As coal mining progressed, when the rock and soil's comprehensive stress on the sliding surface due to their weight and other forces was more significant than their shear strength, rock and soil masses slid along faults and joint surfaces, resulting in this accident [51].

In order to explore the deformation development trend before the accident, the Kriging interpolation method was employed to estimate the cumulative deformation throughout the monitoring period of Sentinel-1A. Subsequently, the deformation values were extracted at intervals of 10 m along the overall collapse direction as well as the Radarsat-2 monitoring. The results are presented in Figure 11. The deformation trends observed in the two datasets were contrasting. Specifically, the monitoring period of Sentinel-1A revealed a clear demarcation between the edge of the collapse trailing edge and the non-collapse area, with deformation gradually diminishing from the boundary towards the interior. In contrast, the monitoring period of Radarsat-2 indicated that the deformation trend progressively increased in size towards the interior.

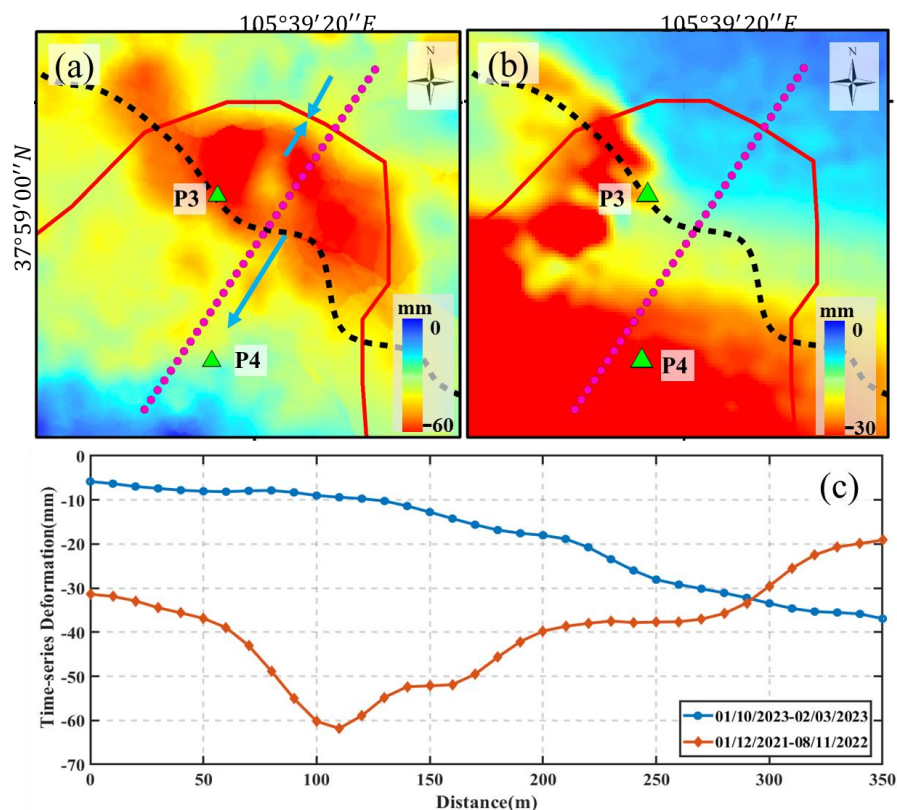


Figure 11. Time-series cumulative deformation diagrams of the collapse trailing edge. (a,b) are the cumulative deformation during the monitoring periods of Sentinel-1A (12 January 2021–11 August 2022) and Radarsat-2 (10 January 2023–3 February 2023), respectively; (c) is the deformation value extracted from the direction of the collapse.

This phenomenon may be attributed to there being faults or joint surfaces between the collapsed area and the non-collapsed area. The entire collapse body was disturbed in the early mining stage, entering the initial creep deformation stage. Consequently, tensile cracks formed at the boundary, leading to larger deformation than in the interior. After a certain period, the collapse body gradually developed and started sliding downward as a cohesive unit. During this stage, the center of the collapse gravity gradually decreased. Meanwhile, due to the influence of terrain and other factors, the deformation rate inside the collapse was greater than at the collapse boundary, and the deformation trend gradually increased downward [52,53]. Figure 10b shows that this transition occurred around 19 January 2022. It also explains why the deformation rate of point P3 was larger than that of point P4.

5.2. Other Potential Causes

The collapse was influenced by a combination of various factors. In addition to human factors, this accident may also have been affected by temperature, coal fires, and old mined-out areas. Specifically, up until 20 February 2023, the local temperature remained relatively stable. However, on 21 February 2023, the average temperature sharply increased by 14 °C (as shown in Figure 12). The moisture in the soil may have thawed due to the abrupt rise in temperature, causing the soil to become loose and reducing both frictional angle and cohesion. Furthermore, in the early stages, the mine underwent underground mining, resulting in the formation of old mined-out areas. Additionally, the coal mine experienced coal fires. The existing voids and coal fires further diminished the mechanical properties of the rock and soil in the mining area, possibly serving as the indirect causes of the accident.

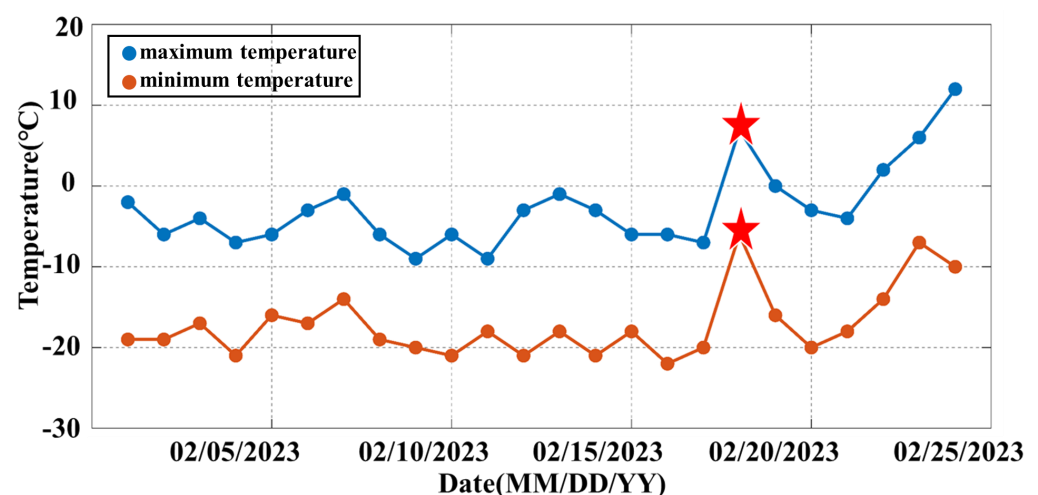


Figure 12. The temperature in Alxa Left Banner, Inner Mongolia, in February 2023 [54] (the red pentagram indicates the temperature on the day before the collapse (21 February 2023)).

5.3. The Other Applications of Multi-Source Remote Sensing of Open-Pit Mines

Multi-source remote sensing data are widely used in the field of open-pit mining. In addition to providing a basis for pre-disaster warning and post-disaster rescue in this study, it could also be used for intelligent identification and land cover classification of open-pit mines by employing high-resolution optical data through artificial intelligence methods such as neural networks [55,56]. Furthermore, the activities of open-pit mines could be identified by the coherence and deformation information obtained from InSAR data [57,58]. Multi-source remote sensing data can play a crucial role in environmental impact assessment, illegal mining detection, and practical mining management in the open-pit mining field.

5.4. Challenging Issues and Future Research

It is worth noting that the deformation caused by open-pit mining contains three-dimensional information, while single-platform SAR can only obtain one-dimensional defor-

mation information along the line of sight [59], leading to certain limitations in slope stability monitoring. Additionally, significant ground disturbances caused by open-pit mining result in low coherence in some areas, thereby hindering the accuracy of InSAR measurements.

Furthermore, despite the advantages of satellite remote sensing, such as short revisit periods and wide coverage, the real-time monitoring demands for open-pit mines are still challenging for current satellites. Moreover, the accessible Sentinel-1A data have relatively low resolution, making it difficult to fulfill the requirements for fine-scale monitoring of open-pit mines. This issue could be partially solved by high-resolution remote sensing data. However, the cost is relatively high due to the long-term monitoring period. Meanwhile, data gaps are prone to occur during the monitoring.

To achieve the goal of real-time monitoring of open-pit mines, multi-source data, including multi-platform InSAR data, geological radar, GNSS, etc., can be utilized to restore the information for missing periods and obtain the three-dimensional deformation through employing artificial intelligence algorithms such as deep learning algorithms. This will be our future research focus.

6. Conclusions

In this study, the temporal and spatial variation characteristics of the dump slopes and collapse area before and after the accident in the Xinjing Open-Pit Mine in Inner Mongolia, China, were analyzed by extensively employing the multi-source remote sensing data of GF-2, Sentinel-1A, and Radarsat-2. The collapse area was accurately and quickly delineated by employing remote sensing interpretation, measuring approximately 630 m in length from north to south and 520 m in width from east to west. Using Radarsat-2 data from 20 days before the accident and D-InSAR technology, the maximum deformation range of the open-pit mine was found to be about -80 mm. Analysis of the collapse area profile line revealed an irregular overall deformation trend, potentially related to the mining activities. The time-series deformation was obtained by the DS-InSAR method based on Sentinel-1A data, and the cumulative deformation of the dump slopes ranged from -60 mm to -80 mm. The cumulative deformation and velocity of the dump typical feature points showed a linear trend.

All these suggest that the dumps were stable overall. Furthermore, a distinct dividing line of deformation between the collapse trailing edge and non-collapsed areas was identified, and the collapse trailing edge boundary could be distinguished. The deformation trends of the collapse trailing edge exhibited opposing patterns during the monitoring periods of Sentinel-1A and Radarsat-2. The possible explanation for this disparity is that they were applied at different stages of the collapse. Finally, the causes of the accident were analyzed. The main cause was that the construction was not carried out according to the preliminary design, while the thawing of soil moisture caused by an increase in temperature and the reduction in the mechanical properties of the rock and soil due to underground voids and coal fires were secondary factors.

Optical remote sensing could be used to accurately and quickly delineate the collapse area after a disaster, and radar remote sensing could be employed for pre-disaster warning. Large-scale open-pit mines could be continuously monitored in real time by integrating various remote sensing technologies. This comprehensive approach enables efficient and accurate detection of open-pit mines, thus mitigating the risk of potential geological disasters.

Author Contributions: Conceptualization, N.Z., Y.W., and F.Z.; methodology, N.Z., H.F., S.Y. and W.Z.; investigation, W.K., X.D. and D.Z.; data curation, N.Z., R.S. and T.W.; writing—original draft preparation, N.Z.; writing—review and editing, N.Z., T.W., K.Z., F.Z., L.Z. and Y.W.; visualization, N.Z.; supervision, N.Z. All authors have read and agreed to the published version of the manuscript.

Funding: This research was supported in part by the National Natural Science Foundation of China (Grant No. 41874044), China Postdoctoral Science Foundation (Grant No. 2023T160685 and Grant No. 2020M671646), Young Elite Scientists Sponsorship Program by CAST (Grant No. YESS20230599),

National Natural Science Foundation of China (Grant No. 42004011 and Grant No. 52104174), Xinjiang Key Research and Development Program (Grant No. 2022B03003-1).

Conflicts of Interest: The authors declare no conflicts of interest.

References

1. Chen, Y.; Li, M.; Pu, H.; Ju, F.; Zhang, K.; Wu, H. Experimental study on dynamic mechanical characteristics of coal specimens considering initial damage effect of cyclic loading. *J. China Coal Soc.* **2023**, *48*, 2123–2137.
2. Liu, L.; Guo, E.; Li, Z.; Zhou, P. Suggestions on strengthening the environmental management in open-pit coal mines during the 14th Five-Year Plan. *China Coal* **2021**, *10*, 61–66.
3. Du, S.; Saroglou, C.; Chen, Y.; Lin, H.; Yong, R. A new approach for evaluation of slope stability in large open-pit mines: A case study at the Dexing Copper Mine, China. *Environ. Earth Sci.* **2022**, *81*, 102. [[CrossRef](#)]
4. Nie, L.; Li, Z.; Zhang, M.; Xu, L. Deformation characteristics and mechanism of the landslide in West Open-Pit Mine, Fushun, China. *Arab. J. Geosci.* **2015**, *8*, 4457–4468. [[CrossRef](#)]
5. Gama, F.F.; Cantone, A.; Mura, J.C.; Pasquali, P.; Paradella, W.R.; dos Santos, A.R.; Silva, G.G. Monitoring subsidence of open pit iron mines at Carajás Province based on SBAS interferometric technique using TerraSAR-X data. *Remote Sens. Appl. Soc. Environ.* **2017**, *8*, 199–211. [[CrossRef](#)]
6. Bond, J.; Chrzanowski, A.; Wilkins, R. Using GPS for augmenting deformation monitoring systems in open pit mines-problems and solutions. *Geomatica* **2005**, *59*, 73–82.
7. Shan, Z.; Han, H.; Jiang, K. Optimization model of GNSS/pseudolites structure design for open-pit mine positioning. *Trans. Nonfer. Met. Soc. China* **2013**, *23*, 2201–2208. [[CrossRef](#)]
8. Dick, G.J.; Eberhardt, E.; Cabrejo-Liévano, A.G.; Stead, D.; Rose, N.D. Development of an early-warning time-of-failure analysis methodology for open-pit mine slopes utilizing ground-based slope stability radar monitoring data. *Can. Geotech. J.* **2015**, *52*, 515–529. [[CrossRef](#)]
9. Poyraz, B.; Yavuz, G.; Poyraz, F. Evaluation of the monitoring of surface deformations in open-pit mines with Sentinel-1A satellite radar data. *J. Sci. Rep. A* **2023**, *54*, 194–211. [[CrossRef](#)]
10. Gama, F.F.; Cantone, A.; Mura, J.C. Monitoring horizontal and vertical components of SAMARCO mine dikes deformations by DInSAR-SBAS using TerraSAR-X and Sentinel-1 Data. *Mining* **2022**, *2*, 725–745. [[CrossRef](#)]
11. Du, S.; Wang, Y.; Zheng, M.; Zhou, D.; Xia, Y. Goaf locating based on InSAR and probability integration method. *Remote Sens.* **2019**, *11*, 812. [[CrossRef](#)]
12. Xia, Y.; Wang, Y. InSAR and PIM based inclined goaf determination for illegal mining detection. *Remote Sens.* **2020**, *12*, 3884. [[CrossRef](#)]
13. Wu, P.C.; Wei, M.; D’Hondt, S. Subsidence in coastal cities throughout the world observed by InSAR. *Geophys. Res. Lett.* **2022**, *49*, e2022GL098477. [[CrossRef](#)]
14. Henderson, S.; Pritchard, M. Decadal volcanic deformation in the Central Andes Volcanic Zone revealed by InSAR time series. *Geochem. Geophys. Geosys.* **2013**, *14*, 1358–1374. [[CrossRef](#)]
15. Zhang, X.; Feng, M.; Zhang, H.; Wang, C.; Tang, Y.; Xu, J.; Yan, D.; Wang, C. Detecting rock glacier displacement in the central himalayas using multi-temporal InSAR. *Remote Sens.* **2021**, *13*, 4738. [[CrossRef](#)]
16. Jarosz, A.; Zahiri, H. Interferometric synthetic aperture radar (InSAR) and its potential to monitor subsidence over caving zones induced by underground mining. *Future Min.* **2008**, pp. 143–149.
17. Yang, F.; Shao, Y.; Ma, G. Application research of InSAR technology used to monitor the slope deformation in Haizhou open-pit mine. *Sci. Surv. Mapp.* **2009**, *34*, 56–58.
18. He, X.; Gao, Z.; Xiao, R.; Luo, H.; Jia, D.; Zhang, Z. Application and prospect of the integration of InSAR and BDS/GNSS for land surface deformation monitoring. *Acta Geod. Cartogr. Sin.* **2022**, *51*, 1338.
19. Yan, S.; Ruan, Z.; Liu, G.; Deng, K.; Lv, M.; Perski, Z. Deriving ice motion patterns in mountainous regions by integrating the intensity-based pixel-tracking and phase-based D-InSAR and MAI approaches: A case study of the Chongce glacier. *Remote Sens.* **2016**, *8*, 611. [[CrossRef](#)]
20. Ferretti, A.; Prati, C.; Rocca, F. Nonlinear subsidence rate estimation using permanent scatterers in differential SAR interferometry. *IEEE Trans. Geosci. Remote Sens.* **2000**, *38*, 2202–2212. [[CrossRef](#)]
21. Khoshlahjeh Azar, M.; Hamedpour, A.; Maghsoudi, Y.; Perissin, D. Analysis of the deformation behavior and sinkhole risk in Kerdabad, Iran using the PS-InSAR method. *Remote Sens.* **2021**, *13*, 2696. [[CrossRef](#)]
22. Berardino, P.; Fornaro, G.; Lanari, R.; Sansosti, E. A new algorithm for surface deformation monitoring based on small baseline differential SAR interferograms. *IEEE Trans. Geosci. Remote Sens.* **2002**, *40*, 2375–2383. [[CrossRef](#)]
23. Zhao, R.; Li, Z.; Feng, G.; Wang, Q.; Hu, J. Monitoring surface deformation over permafrost with an improved SBAS-InSAR algorithm: With emphasis on climatic factors modeling. *Remote Sens. Environ.* **2016**, *184*, 276–287. [[CrossRef](#)]
24. Cao, N.; Lee, H.; Jung, H.C. Mathematical framework for phase-triangulation algorithms in distributed-scatterer interferometry. *IEEE Geosci. Remote Sens. Lett.* **2015**, *12*, 1838–1842.
25. Du, Y.; Yan, S.; Yang, H.; Jiang, J.; Zhao, F. Investigation of deformation patterns by DS-InSAR in a coal resource-exhausted region with Spaceborne SAR imagery. *J. Asian Earth Sci.* **2021**, *5*, 100049. [[CrossRef](#)]

26. Zhao, C.; Li, Z.; Tian, B.; Zhang, P.; Chen, Q. A ground surface deformation monitoring InSAR method using improved distributed scatterers phase estimation. *IEEE J. Sel. Top. Appl. Earth Obs. Remote Sens.* **2019**, *12*, 4543–4553. [[CrossRef](#)]
27. Li, M.; Zhang, S.; Gao, Y. Optimized DS-InSAR technology for time series deformation monitoring in open-pit mines. *Met. Mine* **2023**, *1*, 110–118.
28. Ding, L.; Cai, X.; Liu, L.; Ma, L.; Zhou, W. Effect of weak interlayer on slope stability of open-pit mine. *Met. Mine* **2012**, *4*, 40–42.
29. Zhan, Q.; Sun, X.; Li, C.; Zhao, Y.; Zhou, X.; He, Y.; Zhang, Y.; et al. Stability analysis and reinforcement of a high-steep rock slope with faults: Numerical analysis and field monitoring. *Adv. Civ. Eng.* **2019**, *2019*, 3732982. [[CrossRef](#)]
30. Wang, X.; Guan, X.; Wang, X.; Zhang, P.; Yue, P. Study on stability of open-pit mine slope and sensitivity of rock mass parameters. *J. China Coal Soc.* **2011**, *36*, 1806–1811.
31. Xing, Z.; Peng, S.; Du, W.; He, Y.; Chong, S.; Feng, F.; Yu, P.; She, C.; Xu, D. Hydrogeological changes caused by opencast coal mining in steppe zone: A case study of Shengli 1 open-pit coal mine. *Desalin. Water Treat.* **2018**, *121*, 126–133. [[CrossRef](#)]
32. Pathan, S.M.; Pathan, A.G.; Siddiqui, F.I.; Memon, M.B.; Soomro, M.H.A.A. Open pit slope stability analysis in soft rock formations at Thar Coalfield Pakistan. *Arch. Min. Sci.* **2022**, *67*, 437–454.
33. Jiang, S.; Li, J.; Zhang, S.; Gu, Q.; Lu, C.; Liu, H. Landslide risk prediction by using GBRT algorithm: Application of artificial intelligence in disaster prevention of energy mining. *Process Saf. Environ. Prot.* **2022**, *166*, 384–392. [[CrossRef](#)]
34. Jiang, N.; Zhou, C.; Lu, S.; Zhang, Z. Propagation and prediction of blasting vibration on slope in an open pit during underground mining. *Tunn. Undergr. Space Technol.* **2017**, *70*, 409–421. [[CrossRef](#)]
35. Guo, H.; Gong, C. Study on stability relationship of slope under different cross section forms in Heishan Open-pit Mine. *Opencast Min. Technol.* **2023**, *38*, 56–60.
36. Mura, J.C.; Paradella, W.R.; Gama, F.F.; Silva, G.G.; Galo, M.; Camargo, P.O.; Silva, A.Q.; Silva, A. Monitoring of non-linear ground movement in an open pit iron mine based on an integration of advanced DInSAR techniques using TerraSAR-X data. *Remote Sens.* **2016**, *8*, 409. [[CrossRef](#)]
37. Yang, T.; Zhang, F.; Yu, Q.; Cai, M.; Li, H. Research situation of open-pit mining high and steep slope stability and its developing trend. *Rock Soil Mech.* **2011**, *32*, 1437–1451.
38. Ministry of Emergency Management of the People's Republic of China. Available online: <https://www.mem.gov.cn> (accessed on 29 August 2023).
39. Wu, H.; Zhang, Y.; Kang, Y.; Wei, J.; Liu, Y.; Li, B. *Fine Mapping of Surface Deformation in Xinjing Open-Pit Mine, Inner Mongolia Using FS-InSAR Technique*; Geomatics and Information Science of Wuhan University: Wuhan, China, 2023.
40. An, B.; Wang, C.; Liu, C.; Li, P. A multi-source remote sensing satellite view of the February 22nd Xinjing landslide in the mining area of Alxa left Banner, China. *Landslides* **2023**, *20*, 2517–2523. [[CrossRef](#)]
41. Natural Resources Satellite Remote Sensing Service Cloud Platform. Available online: <https://www.sasclouds.com> (accessed on 2 March 2023).
42. Canadian Space Agency. Available online: <https://www.asc-csa.gc.ca/eng> (accessed on 2 March 2023).
43. Alaska Satellite Facility (ASF). Available online: [Availableonline:https://www.asf.alaska.edu](https://www.asf.alaska.edu) (accessed on 2 May 2023).
44. Wang, T.; Zhao, F.; Wang, Y.; Zhang, N.; Zhou, D.; Diao, X.; Zhao, X. An Algorithm for Locating Subcritical Underground Goaf Based on InSAR Technique and Improved Probability Integral Model. *IEEE Trans. Geosci. Remote Sens.* **2023**, *61*, 1–14. [[CrossRef](#)]
45. Fan, H.; Deng, K.; Ju, C.; Zhu, C.; Xue, J. Land subsidence monitoring by D-InSAR technique. *Min. Sci. Technol.* **2011**, *21*, 869–872. [[CrossRef](#)]
46. Chen, Y.; Li, J.; Li, H.; Gao, Y.; Li, S.; Chen, S.; Guo, G.; Wang, F.; Zhao, D.; Zhang, K.; et al. Revealing land surface deformation over the Yineng Backfilling Mining Area, China, by integrating Distributed Scatterer SAR Interferometry (DS InSAR) and a Mining Subsidence Model. *IEEE J. Sel. Top. Appl. Earth Obs. Remote Sens.* **2023**, *16*, 3611–3634. [[CrossRef](#)]
47. Li, T.; Zhang, H.; Fan, H.; Zheng, C.; Liu, J. Position inversion of goafs in deep coal seams based on DS-InSAR data and the probability integral methods. *Remote Sens.* **2021**, *13*, 2898. [[CrossRef](#)]
48. Jiang, M.; Ding, X.; Hanssen, R.F.; Malhotra, R.; Chang, L. Fast statistically homogeneous pixel selection for covariance matrix estimation for multitemporal InSAR. *IEEE Trans. Geosci. Remote Sens.* **2014**, *53*, 1213–1224. [[CrossRef](#)]
49. Peng, K.; Zhao, F.; Wang, Y.; Yan, S.; Feng, H. DS-InSAR phase optimization based on singular value decomposition. *Natl. Remote Sens. Bull.* **2023**, *27*, 533–542. [[CrossRef](#)]
50. Wang, Z. *Landslide Remote Sensing*; Science Press: Beijing, China, 2012; pp. 97–110.
51. Cai, M.; Heng, M.; Liu, D. *Rock Mechanics and Engineering*; Science Press: Beijing, China, 2013; pp. 362–371.
52. Yang, T.; Wang, H.; Dong, X.; Liu, F.; Zhang, P.; Deng, W. Current situation, problems and countermeasures of intelligent evaluation of slope stability in open pit. *J. China Coal Soc.* **2020**, *45*, 2277–2295.
53. Intrieri, E.; Carlà, T.; Farina, P.; Bardi, F.; Ketizmen, H.; Casagli, N. Satellite interferometry as a tool for early warning and aiding decision making in an open-pit mine. *IEEE J. Sel. Top. Appl. Earth Obs. Remote Sens.* **2019**, *12*, 5248–5258. [[CrossRef](#)]
54. China Meteorological Administration. Available online: <https://www.cma.gov.cn/> (accessed on 28 February 2023).
55. Xie, H.; Pan, Y.; Luan, J.; Yang, X.; Xi, Y. Open-pit mining area segmentation of remote sensing images based on DUSegNet. *J. Indian Soc. Remote Sens.* **2021**, *49*, 1257–1270. [[CrossRef](#)]
56. Chen, T.; Hu, N.; Niu, R.; Zhen, N.; Plaza, A. Object-oriented open-pit mine mapping using Gaofen-2 satellite image and convolutional neural network, for the Yuzhou City, China. *Remote Sens.* **2020**, *12*, 3895. [[CrossRef](#)]

57. Moon, J.; Lee, H. Analysis of activity in an open-pit mine by using InSAR coherence-based normalized difference activity index. *Remote Sens.* **2021**, *13*, 1861. [[CrossRef](#)]
58. Hartwig, M.E.; Paradella, W.R.; Mura, J.C. Detection and monitoring of surface motions in active open pit Iron mine in the Amazon region, using persistent scatterer interferometry with TerraSAR-X satellite data. *Remote Sens.* **2013**, *5*, 4719–4734. [[CrossRef](#)]
59. Hu, J.; Li, Z.; Ding, X.; Zhu, J.; Zhang, L.; Sun, Q. Resolving Three-dimensional Surface Displacements from InSAR measurements: A review. *Earth-Sci. Rev.* **2014**, *133*, 1–17. [[CrossRef](#)]

Disclaimer/Publisher’s Note: The statements, opinions and data contained in all publications are solely those of the individual author(s) and contributor(s) and not of MDPI and/or the editor(s). MDPI and/or the editor(s) disclaim responsibility for any injury to people or property resulting from any ideas, methods, instructions or products referred to in the content.